Progress in Nuclear Energy 99 (2017) 59–72

Contents lists available at ScienceDirect

Progress in Nuclear Energy

journal homepage: www.elsevier.com/locate/pnucene

# Rhenium resonance parameters from neutron capture and transmission measurements in the energy range 0.01 eV to 1 keV

B.E. Epping [a, c, *], G. Leinweber [a], D.P. Barry [a], M.J. Rapp [a], R.C. Block [a], T.J. Donovan [a], Y. Danon [b], S. Landsberger [c]

[a] Naval Nuclear Laboratory, Knolls Atomic Power Laboratory, P.O. Box 1072, Schenectady, NY 12301-1072, United States
[b] Rensselaer Polytechnic Institute, Gaerttner LINAC Center, 110 8th St, Troy, NY 12180, United States
[c] The University of Texas at Austin, Nuclear Engineering Teaching Lab, Pickle Research Campus, R-9000, Austin, TX 78712, United States

ARTICLE INFO

*Article history:*
Received 16 June 2016
Received in revised form
21 March 2017
Accepted 17 April 2017
Available online 8 May 2017

*Keywords:*
Rhenium
$^{185}$Re
$^{187}$Re
Transmission
Capture yield
Resonance parameters
Resonance integral
Thermal cross section
NNL
RPI
LINAC

ABSTRACT

Rhenium is a refractory metal with potential uses in nuclear reactor applications, particularly those at very high temperatures. Measurements have been made using natural samples. Natural rhenium consists of two isotopes: $^{185}$Re (37.40%) and $^{187}$Re (62.60%). The electron linear accelerator (LINAC) at the Rensselaer Polytechnic Institute (RPI) Gaerttner LINAC Center was used to explore neutron interactions with rhenium in the energy region from 0.01 eV to 1 keV. Neutron capture and transmission measurements were performed by the time-of-flight technique. Two transmission measurements were performed at flight paths of 15 m and 25 m with $^{6}$Li glass scintillation detectors. The neutron capture measurements were performed at a flight path of 25 m with a 16-segment sodium iodide multiplicity detector. Resonance parameters were extracted from the data using the multilevel R-matrix Bayesian code SAMMY. A table of resonance parameters and their uncertainties is presented. The uncertainties in resonance parameters were propagated from a number of experimental quantities using a Bayesian analysis. Uncertainties were also estimated from fitting each Re sample measurement individually. The measured neutron capture resonance integral for $^{185}$Re is (4 ± 1)% larger than ENDF/B-VII.1. The capture resonance integral for $^{187}$Re is (3 ± 1)% larger than ENDF/B-VII.1. Other findings from these measurements include: a decrease in the thermal capture cross section for $^{185}$Re of (2 ± 2)% from ENDF/B-VII.1; a decrease in the thermal capture cross section for $^{187}$Re of (3 ± 4)% from ENDF/B-VII.1; a decrease in the thermal total cross section for $^{185}$Re of (2 ± 2)% from ENDF/B-VII.1; and a decrease in the thermal total cross section for $^{187}$Re of (6 ± 5)% from ENDF/B-VII.1. Considering the uncertainties, none of the indicated changes in thermal cross sections represents a statistically significant change from ENDF/B-VII.1.



## 1. Introduction

Rhenium is an extremely rare material that does not occur as a free element in nature. It is extremely dense, has a high melting point, and the highest boiling point of any element (Weast et al., 1987). Natural rhenium consists of one stable isotope, $^{185}$Re (37.40% abundance) and one long-lived isotope, $^{187}$Re (62.60% abundance; half-life of 4.12 × $10^{10}$ years)(Baum et al., 2010). As a refractory metal (i.e., extremely resistant to heat and wear), rhenium has potential uses in reactor applications(Friesenhahn et al. 1967). Alloys containing rhenium have potential use in space reactors and fusion reactors (Busby et al., 2007; Craft et al., 2014; Guan et al., 2016).

The purpose of the present work was to determine resonance parameters for rhenium. The resonance parameters in ENDF/B-VII.1 (Chadwick et al., 2011) were adopted from Mughabghab (Mughabghab, 2006). The values published by Mughabghab are based on several historical experiments.

The earliest measurements of rhenium resonance parameters were performed by Melkonian et al. (1953) who performed neutron transmission measurements in natural rhenium samples up to 21.2 eV at Columbia University in 1953. Two years later, Igo (1955)



* Corresponding author. Naval Nuclear Laboratory, Knolls Atomic Power Laboratory, P.O. Box 1072, Schenectady, NY 12301-1072, United States.
*E-mail address:* brian.epping@unnpp.gov (B.E. Epping).

http://dx.doi.org/10.1016/j.pnucene.2017.04.015
0149-1970/

conducted neutron transmission measurements between 1 eV and 13 eV with natural rhenium samples using the crystal spectrometer at Brookhaven National Laboratory. In 1965, Vertebnyi et al. (1965) performed neutron transmission measurements up to 110 eV with isotopically enriched samples of $^{185}$Re and $^{187}$Re along with natural rhenium using the VVR-M reactor with a chopper and published resonance parameters up to 21.46 eV. Friesenhahn et al. (1967) performed neutron transmission, capture yield, and self-indication measurements in 1967 with natural rhenium samples using the Gulf General Atomic linear accelerator for energies up to 30 keV, with resonance parameters evaluated up to 100 eV. Ideno et al. (1972) performed neutron transmission measurements in 1971 with natural rhenium samples using the linear accelerator at the Japan Atomic Energy Research Institute up to 300 eV. In 1976, Namenson et al. (1976) measured neutron resonance parameters up to 2 keV in isotopically enriched rhenium samples using the Oak Ridge National Laboratory linear accelerator (ORELA). More recently (2012), Arboccò et al. (2013) measured the thermal total cross sections of $^{185}$Re and $^{187}$Re as part of neutron activation analyses performed at the Belgian Reactor 1 at Studiecentrum voor Kernenergie – Centre d'étude de l'énergie nucléaire (BR1, SCK•CEN).

## 2. Experimental conditions

### 2.1. Overview

The RPI LINAC was used to accelerate electrons into one of the tantalum neutron-producing targets. Bremsstrahlung radiation and photoneutrons were produced. The neutron-producing targets were optimized for each energy range (Danon et al., 1993; Danon et al., 1995; Overberg et al., 1999). Thermal and epithermal capture and epithermal transmission were measured at a 25 m flight path. Thermal transmission was measured at 15 m. Thermal and epithermal transmission were measured with $^{6}$Li glass detectors (Barry, 2003; Leinweber et al., 2002, 2010; Trbovich, 2003). Thermal and epithermal capture were measured with a 16-segment NaI detector (Barry, 2003; Leinweber et al., 2002, 2010; Trbovich, 2003; Block et al., 1988).

Table 1 gives some details of the experimental conditions including neutron targets, overlap filters (used to prevent overlap of neutron pulses by removing the lowest energy neutrons from each pulse), LINAC pulse repetition rates, flight path lengths, and time-of-flight channel widths. The neutron energy for a detected event was determined using the time-of-flight (TOF) technique. The nominal resolution, pulse width divided by flight path length, was ≈1.8 ns/m for epithermal transmission and capture measurements.

Table 2 gives some sample information including the sample thicknesses and measurements for which each sample was used. The uncertainties in sample thickness were propagated from multiple measurements of sample mass and diameter. The diameter measurements were the dominant component of the uncertainties in the number densities. All samples were mounted in open aluminum sample cans. The influence of these sample cans, as well as all background, was measured by including empty sample cans in all measurements. Background in transmission measurements is discussed in Section 3.2.1.

An independent array of neutron detectors was used to monitor for fluctuations in LINAC operation. These detectors, referred to as beam monitors or monitors, were used to perform statistical checks of the measured data, and one monitor was selected as the beam intensity normalization standard for each experiment.

### 2.2. Sample information

There are only two naturally-occurring isotopes of rhenium, $^{185}$Re and $^{187}$Re. The samples used in the current measurements were elemental and in metallic form. The samples were obtained from Rhenium Alloys, Inc. and were certified >99.99% pure rhenium. The results of impurity analyses performed on the rhenium samples by the vendor are given in Table 3.

### 2.3. Capture detector

The capture detector is a gamma ray detector containing 20 cubic decimeters of NaI(Tl) divided into 16 optically-isolated segments (Block et al., 1988). The scintillation crystals form an annulus around the neutron beam with the sample at its center. The neutron beam was collimated to a diameter of 5.08 cm at the sample position. Neutrons that scatter from the sample are absorbed by a hollow cylindrical liner (0.9 cm thick) fabricated of 98.4 wt% $^{10}B_4C$ ceramic to reduce the number of scattered neutrons reaching the gamma detector. The discriminator on each detector section was set to 100 keV. A total energy deposition of 1 MeV for the epithermal measurement and 2 MeV for the thermal measurement was required to register a capture event. Therefore, the system discriminates against the 478 keV gamma rays from $^{10}$B(n;α,γ)

**Table 1**
Rhenium experimental details.

| Experiment | Overlap Filter | Neutron-Producing Target | Elec-tron Pulse Width (ns) | Ave. Beam Current (μA) | Beam Energy (MeV) | Energy Region, (eV) | Channel Width, (μs) | Pulse Repetition Rate (pulses/s) | Flight Path Length (m) |
|---|---|---|---|---|---|---|---|---|---|
| Epithermal Transmission | Boron Carbide | Bare Bounce | 42 ± 2 | 13 | 56 | E < 4.0<br>4.0 < E < 44.4<br>44.4 < E <258.2<br>E > 258.2 | 8.00000<br>0.50000<br>0.06250<br>0.03125 | 225 | 25.596 ± 0.0055 |
| Thermal Transmission | None | Enhanced Thermal Target | 700 ± 50 | 7 | 50 | E < 0.36<br>0.36 < E < 9.00<br>9.00 < E < 36.81<br>E > 36.81 | 16.0000<br>1.0000<br>0.2500<br>0.0625 | 25 | 14.973 ± 0.0055 |
| Epithermal Capture | Cadmium | Bare Bounce | 47.1 ± 0.3 | 16 | 53 | E < 4.0<br>4.0 < E < 44.2<br>44.2 < E < 255.5<br>E > 255.5 | 8.00000<br>0.50000<br>0.06250<br>0.03125 | 225 | 25.564 ± 0.0055 |
| Thermal Capture | None | Enhanced Thermal Target | 860 ± 130 | 6.6 | 48 | E < 0.60<br>0.60 < E < 8.85<br>8.85 < E < 35.61<br>E > 35.61 | 16.0000<br>1.0000<br>0.2500<br>0.1250 | 25 | 25.444 ± 0.0055 |

**Table 2**
Sample details.

| Nominal Thickness | Areal Density (atoms/barn) | Uncertainty (atoms/barn) | Measurements |
|---|---|---|---|
| 0.0254 mm (1 mil; 0.001 in) | 2.0415E-04 | 9E-08 | Thermal transmission, thermal capture |
| 0.0508 mm (2 mil) | 3.657E-04 | 2E-07 | Thermal transmission, epithermal capture, thermal capture |
| 0.127 mm (5 mil) | 8.50E-04 | 2E-06 | Epithermal transmission, epithermal capture |
| 0.254 mm (10 mil) | 1.874E-03 | 2E-06 | Epithermal transmission, thermal transmission, epithermal capture, thermal capture |
| 0.508 mm (20 mil) | 3.790E-03 | 7E-06 | Epithermal transmission, epithermal capture, thermal capture |
| 1.270 mm (50 mil) | 9.062E-03 | 5E-06 | Epithermal transmission, thermal transmission, epithermal capture, thermal capture |
| 2.540 mm (100 mil) | 1.804E-02 | 1E-05 | Thermal transmission |

**Table 3**
Impurities in the rhenium samples.

| Impurities | Concentration of Each Impurity |
|---|---|
| Ag, Al, As, Au, B, Ba, Be, Bi, Ca, Cd, Co, Cr, Cs, Cu, Ga, Ge, Hf, In, Ir, Li, Mn, Nb, Pb, Pd, Pt, Rb, Rh, Ru, Sb, Se, Sn, Sr, Ta, Te, Ti, Tl, U, V, Zn, Zr | <5 ppm |
| Fe, K, Mo, Na, Ni, P, Si, W | <10 ppm |
| Mg | 12 ppm |

reactions.

The efficiency of the capture detector is about 75% for a single 2 MeV gamma ray. The efficiency of detecting a capture event in rhenium is close to 100% since, on average, 3–4 gamma rays are emitted for each capture event.

The samples were precisely positioned at the center of the detector by a computer-controlled sample changer. Each data run consisted of one complete cycle through the samples, with a predetermined number of LINAC pulses for each sample. The distribution of pulses per sample was chosen to minimize the counting statistical error in the measured cross section (Danon & Block, 2005). The dead time of the system was 1.125 μs, and the dead time correction factor was less than 9.1% for the thermal measurement and under 5.1% for epithermal.

### 2.4. Transmission detectors

The epithermal neutron transmission measurement was conducted at the 25 meter flight station. It utilized a 12.70 cm (5 inch) diameter, 1.27 cm thick $^{6}$Li glass scintillator housed in a light-tight aluminum box and viewed by two photomultiplier tubes that are out of the neutron beam. The details of this detector design were documented by Barry (2003). The measurement with this detector covered the range of incident neutron energies from 10 eV to 1 keV.

The thermal transmission measurement was conducted at the 15 meter flight station. The 15 meter flight station contains a 7.62 cm (3 inch) diameter, 0.3 cm thick NE 905 $^{6}$Li glass scintillation detector and was used for measurements covering the energy range from 0.01 eV to 30 eV. The detector is directly coupled to a single photomultiplier tube.

Transmission samples along with empty sample holders, which are used to measure the open-beam count rate, were mounted on an 8-position computer-controlled sample changer. The samples and sample holders were all at room temperature (approximately 293K) during the transmission experiments. The transmission can be expressed as a function that is approximately the ratio of the count rate with a sample in the beam to the count rate with samples removed. The transmission can vary strongly with incident neutron energy and is directly linked to the total cross section of the sample material being measured. Each data run consisted of one complete cycle through the samples, with a predetermined number of LINAC pulses for each sample position. The distribution of pulses per sample position was chosen to minimize the counting statistical error in the measured cross section (Danon & Block, 2002). The dead time correction factor was less than 2.0% for the epithermal measurement and under 1.2% for the thermal measurement.

## 3. Data reduction

### 3.1. Capture data

Processed capture data are expressed as yield. Yield is defined as the number of neutron captures per neutron incident on the sample. The capture yield, $Y_i$, in time-of-flight channel $i$, is calculated by:

$$Y_i = \frac{C_i - B_i}{K(\varphi_i - B_{\varphi_i})} \quad (1)$$

Where:

$C_i$ is the dead-time-corrected and monitor-normalized counting rate of the sample measurement,
$B_i$ is the dead-time-corrected and monitor-normalized background counting rate,
$K$ is the product of the flux normalization factor and efficiency, and
$\varphi_i$ is the measured neutron flux shape.
$B_{\varphi_i}$ is the dead-time-corrected and monitor-normalized background counting rate in the measured flux shape.

In addition to the sample data, another set of data was needed to determine the energy profile of the neutron flux. This was done by mounting a 2.54 mm thick $B_4C$ sample, enriched to 98.4% $^{10}$B, in the sample changer and adjusting the total energy threshold to record the 478 keV gamma rays from neutron absorption in $^{10}$B. These flux data were corrected for transmission and multiple scattering in the boron sample. The thermal flux was smoothed using 51-point adjacent averaging. The epithermal flux contained the complex structure of the cadmium filter and was not smoothed.

The magnitude of the flux was normalized to a saturated (black) capture resonance, the 2.16 eV resonance in $^{185}$Re. Due to the high gamma attenuation of rhenium, the neutron flux normalization was sample thickness dependent, see Fig. 1. The only samples which were not saturated at 2.16 eV were the 0.0508 mm (2 mil) and the 0.0254 mm (1 mil) samples. Their normalizations were determined from an exponential extrapolation with sample thickness of the saturated samples, see Fig. 2. Subsequent SAMMY evaluations revealed a normalization discrepancy between transmission and capture data sets. This was attributed to the high density of the rhenium samples, which results in significant self-shielding and a resultant under detection of capture photons. To correct this, SAMMY was used to calculate a normalization correction factor for capture yield data based on the transmission results. This factor was determined to be 1.04 and was applied to all

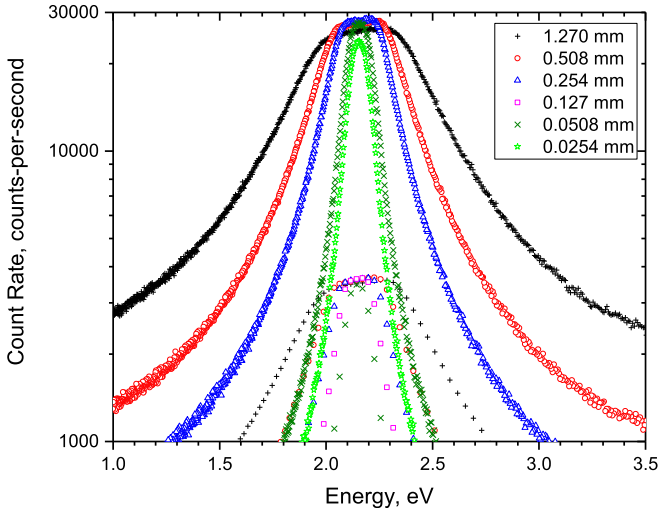


**Fig. 1.** Re sample count rates at the 2.16 eV resonance used for neutron capture flux normalization. The upper group is the thermal data. Many of the same sample thicknesses are also shown in the lower group, the epithermal data. The thermal data have greater density of points due to higher count rates. The four thickest samples are saturated at this resonance, which gives a point to normalize the neutron flux (not shown). The normalization of the flux to saturated capture in Re is sample thickness dependent due to the very high gamma attenuation in Re. The two thinnest samples were not saturated. Their normalization was based on an exponential extrapolation with sample thickness from the saturated samples, see Fig. 2.

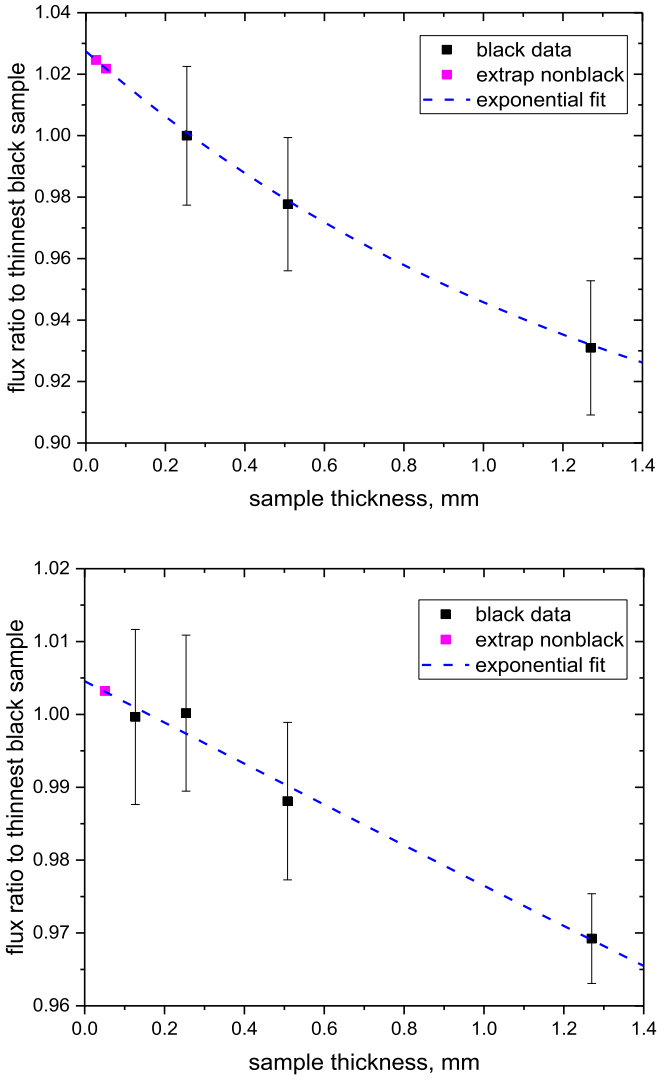


**Fig. 2.** Neutron capture flux normalization factors relative to the thinnest black sample at the 2.16 eV resonance in $^{185}$Re. The normalization factors were sample dependent, see Fig. 1. The thermal data are shown in the top graph. The normalization for the two samples which were not saturated (nonblack) in the 2.16 eV resonance was determined from an exponential extrapolation with sample thickness from the four samples that were saturated; i.e., black. The epithermal data are shown in the bottom graph. The normalization for the only sample which was not saturated in the 2.16 eV resonance was determined from an exponential extrapolation with sample thickness from the four samples that were saturated. The total energy deposition discriminator level for the thermal measurements was 2 MeV, while the total energy deposition discriminator level for the epithermal measurement was 1 MeV.

capture yield data, with satisfactory results.

The zero time-of-flight was obtained from the measured location of the gamma flash resulting from the electron pulse incident on the neutron-producing target.

The background in capture was determined from in-beam measurements of empty sample holders. The capture yield and its associated statistical uncertainty provided input to the SAMMY (Larson, 2008) Bayesian analysis code that extracted the neutron resonance parameters. Systematic components of resonance parameter uncertainties are discussed in Section 4.9.

The signal-to-background ratios for the rhenium capture and transmission measurements are shown in Fig. 3. The value from thermal capture increased from a minimum of ≈50 at 0.01 eV to a local peak of ≈470 near 0.1 eV, and then remained >300 through 30 eV with a maximum value of ≈1000 at 18 eV.

The signal-to-background ratio in the epithermal capture experiment was ≈10 at 0.5 eV and increased almost linearly to ≈300 at 400 eV, remaining essentially constant thereafter.

Further discussion of neutron capture data taking and data reduction techniques at the RPI LINAC were described by Leinweber et al. (2002).

### 3.2. Transmission data

The transmission is given by equation (2).

$$T_i = \frac{\left(C_i^S - K_S B_i - B_S\right)}{\left(C_i^O - K_O B_i - B_O\right)} \tag{2}$$

Where:

$T_i$ is the transmission in time-of-flight channel $i$,
$C_i^S$ and $C_i^O$ are the dead-time corrected and monitor-normalized counting rates of the sample and open measurements in channel $i$, respectively,
$B_i$ is the unnormalized, time-dependent background counting rate in channel $i$,
$B_S$ and $B_O$ are the steady state background counting rates for sample and open measurements, respectively, and
$K_S$ and $K_O$ are the normalization factors for the sample and open background measurements.

The signal-to-background ratios for the transmission measurements are shown in Fig. 3. The value for the epithermal measurement was ≈50 at 10 eV, then rose steadily to a peak of ≈100 near 70 eV, and finally reduced slowly to ≈30 at 1 keV. The large drop in epithermal transmission signal-to-background visible in Fig. 3 near 340 eV resulted from the presence of manganese, which was used as a fixed notch filter as described in the next section. The signal-to-

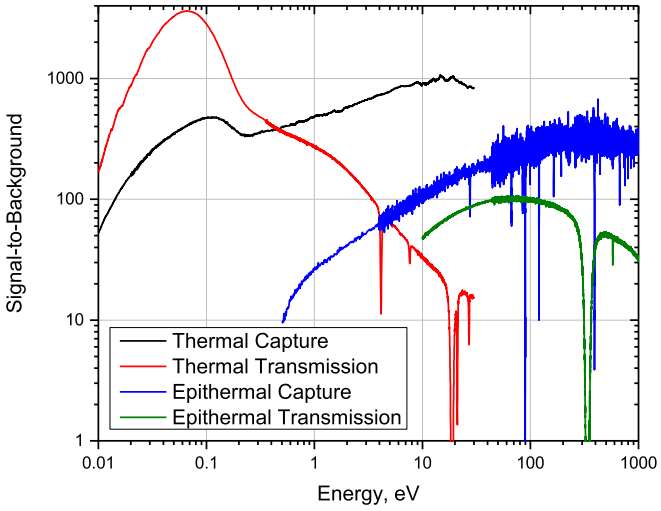


**Fig. 3.** The signal-to-background ratios for the rhenium measurements.

background ratio for the thermal transmission measurement was ≈170 at 0.01 eV, then rose steadily to a peak ≈3000 at 0.07 eV, and finally reduced to ≈15 at 30 eV. The apparent structure in the signal-to-background ratio above 3 eV for the thermal transmission measurement as shown in Fig. 3 resulted from the use of tungsten as the fixed notch filter.

*3.2.1. Transmission background*

Transmission background is a crucial aspect of a total cross section measurement. Transmission background was determined with a fixed notch filter and a dedicated set of measurements employing notch filters. A notch filter is an element with a strong, saturating (or black) resonance at an energy of interest. Any counts observed under a black resonance are attributed to background.

The fixed notch filter for the epithermal transmission measurement was manganese at 336 eV. A separate measurement was performed using a suite of materials with saturating resonances including silver at 5.2 eV, tungsten at 18.8 eV, and cobalt at 132 eV. Single and double thicknesses of these notch filters (including a double-thickness of the fixed notch material) were placed in the beam and measured with each rhenium sample. Since the black resonance in rhenium at 2.16 eV was effectively measured in single and double thicknesses due to the specific sample thicknesses used for the measurements it was also used to help characterize the shape of the background. The one-notch and two-notch data were used to extrapolate to zero-notch thickness (Syme, 1982) The resulting background shape was normalized to the fixed notch at 336 eV.

Thermal transmission time-dependent background was determined from a suite of notch filters including cobalt at 132 eV, tungsten at 18.8 eV, silver at 5.2 eV, indium at 1.46 eV, and Cd at 0.16 eV. The black rhenium resonance at 2.16 eV was also used to help characterize the background shape. The thermal background shape was normalized to the fixed notch of tungsten at 18.8 eV.

## 4. Results

*4.1. Resonance parameters*

Thermal and epithermal neutron capture and transmission experiments were performed to resolve rhenium resonances between 0.01 eV and 1 keV. An overview of the data, the R-matrix Bayesian resonance parameter fit, and ENDF/B-VII.1 is shown in Fig. 4 through Fig. 6. Overall, seven samples were measured in transmission and capture. Sample details are given in Table 2.

Resonance parameters: neutron width, $\Gamma_n$; radiation width, $\Gamma_\gamma$; and resonance energy, E; were extracted from the capture and transmission data sets using the multi-level R-matrix Bayesian code SAMMY version 8 (Larson, 2008). Both capture and transmission data have been fitted to a single set of resonance parameters in the energy range from 0.01 eV to 1000 eV. This was a combined transmission and capture analysis, which employed the experimental resolution, Doppler broadening, self-shielding, and multiple-scattering features of SAMMY. The resulting resonance parameters (up to 100 eV) of $^{185}$Re and $^{187}$Re are listed in Table 4 and Table 5, respectively. In the tables, resonance parameters and their uncertainties are given and compared to ENDF/B-VII.1. The first four columns are resonance energy and uncertainties, the next four columns are radiation width and uncertainties, then four columns of neutron width information, followed by isotope and spin (J). The measured value, the Bayesian and external uncertainties, and the ENDF/B-VII.1 values are given in Tables 4 and 5 for each of the resonance parameters: resonance energy, radiation width, and neutron width.

There are no p-wave resonances for $^{185}$Re and $^{187}$Re listed in ENDF/B-VII.1 in the resolved resonance region; consequently, all of the resonances in $^{185}$Re and $^{187}$Re below 1 keV were treated as s-wave in this analysis, i.e., angular momentum, $\ell = 0$. Furthermore, all resonances were analyzed using the same spin assignments as ENDF/B-VII.1.

The Bayesian uncertainties for each resonance in Tables 4 and 5 were propagated from the multi-sample SAMMY fit of transmission and capture data. Bayesian and external uncertainties are defined and described in Section 4.9 and Section 4.9.8, respectively. The sample-to-sample external uncertainties given in brackets in Tables 4 and 5 for each resonance are an estimate of the consistency within the individual sample data. This external uncertainty is usually larger than the Bayesian error when there are many samples, but above 100 eV the SAMMY uncertainty estimates are often larger. The number of significant figures displayed for the central value of the resonance parameters in Tables 4 and 5 reflects the larger of the two uncertainties.

Better fits using the new resonance parameters were evident throughout the energy spectrum. From 0.01 eV to 0.5 eV, only thermal transmission and thermal capture data were used in the fits. Epithermal capture data were added for the region from 0.5 eV to 10 eV. In the region between 10 and 30 eV all data, epithermal and thermal transmission and capture were included in the fits. Above 30 eV thermal data were not included in the fits due to their poor energy resolution and lack of background information. Epithermal capture data were not included above 600 eV, since the $^{10}$B-enriched $B_4C$ liner of the capture detector is not capable of absorbing all scattered neutrons, and the effects of the resulting undesired neutron interactions in the detector segments become significant at 600 eV. Thus, only epithermal transmission data were used for fits between 600 eV and 1 keV.

The resolved resonance region for rhenium in ENDF/B-VII.1 ends at 2 keV. The current measurements provided improved resonance parameters up to 1 keV. The resonance parameters in the region of 100 eV through 1 keV are documented in Reference (Epping et al., 2017). Examples of the fits resulting from improved resonance parameters are shown in Fig. 7 and Fig. 8. Other important aspects of the analysis included background in transmission, flux normalization in capture, zero-time measurement, and the experimental resolution function. Each of these aspects will be discussed in turn. No external R-function was employed.

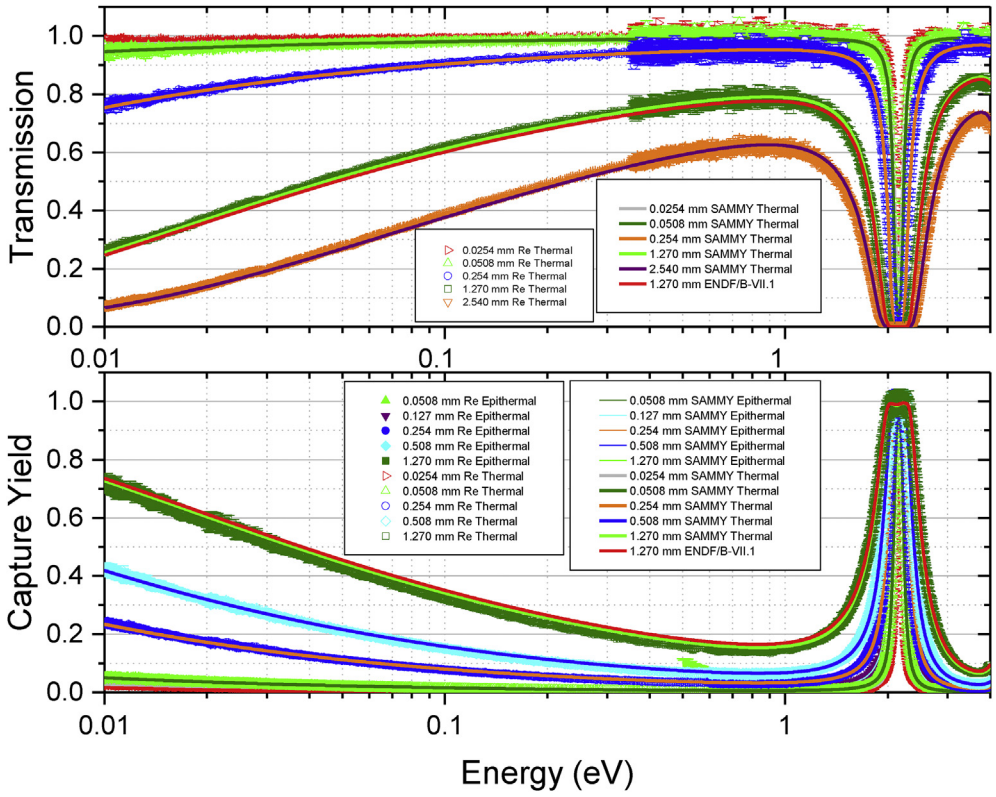


**Fig. 4.** Overview of the NNL/RPI thermal Re data below 4 eV and the resonance parameter fits. A single set of resonance parameters was obtained from the SAMMY fit and used for the curves labeled "SAMMY". Resonance parameters of negative energy resonances were changed to fit the shape of the data in the thermal region. The line derived from ENDF/B-VII.1 for the 1.270 mm (50 mil) sample is included for comparison purposes.

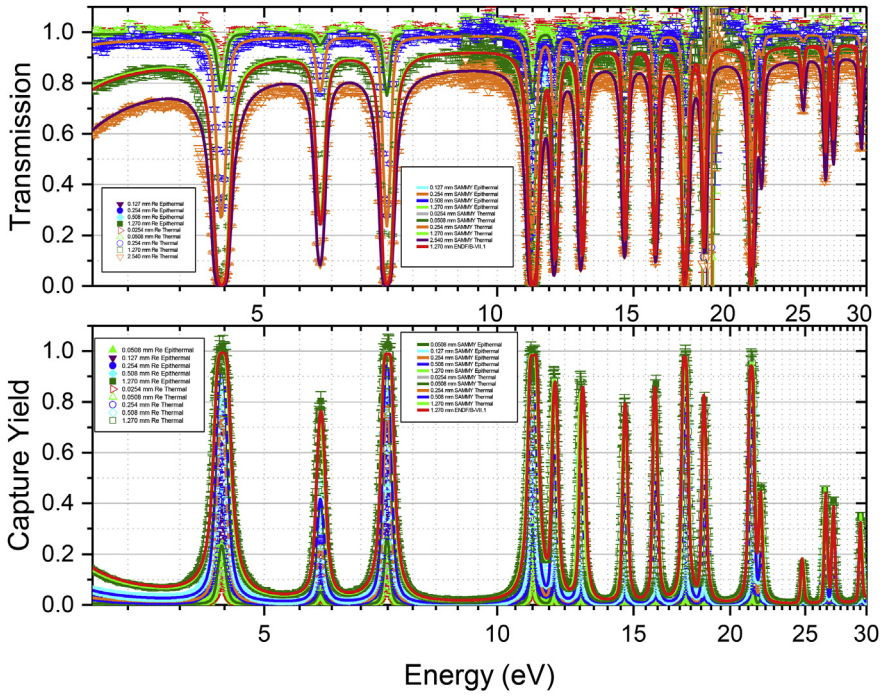


**Fig. 5.** Overview of the NNL/RPI thermal Re data between 3 and 30 eV and the resonance parameter fits. A single set of resonance parameters were obtained from the SAMMY fit and used for the curves labeled "SAMMY". The large uncertainties in the transmission data near 18.8 eV are due to the tungsten fixed notch. The line derived from ENDF/B-VII.1 for the 1.270 mm (50 mil) sample is included for comparison purposes.

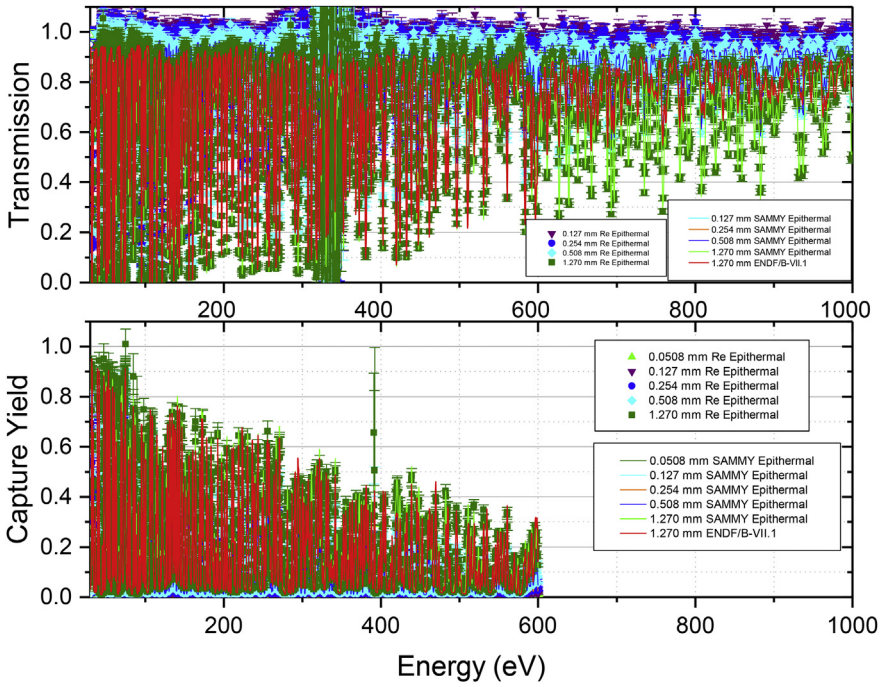


**Fig. 6.** Overview of the NNL/RPI epithermal Re data between 30 and 1000 eV and the resonance parameter fits. A single set of resonance parameters were obtained from the SAMMY fit and used for the curves labeled "SAMMY". The large uncertainties in the transmission data near 336 eV are due to the manganese fixed notch. The large uncertainties in the capture yield data at 392 eV are attributed to the cadmium overlap filter. The line derived from ENDF/B-VII.1 for the 1.270 mm (50 mil) sample is included for comparison purposes.

### 4.2. Transmission background

Background was not fitted during the SAMMY analysis. However, the uncertainty in background was propagated into the transmission uncertainty that was fitted by SAMMY. Background was accounted for in the data processing (described in Section 3.2.1) of each sample's counting spectrum before they were divided, producing transmission. Normalization was not varied in transmission fits.

### 4.3. Capture flux normalization

The neutron flux measurement and sample-dependent normalization for the capture experiment were described in Section 3.1. As previously discussed in Section 3.1, initial SAMMY evaluations revealed a normalization discrepancy between transmission and capture data sets attributed to the high density of the rhenium samples. The discrepancy was subsequently corrected using a normalization correction factor calculated by SAMMY.

### 4.4. Zero time measurement and burst width

The zero mark of each time-of-flight spectrum was observed as a peak in detector counts due to the gamma emission (i.e., the "gamma flash") which accompanies each pulse of neutrons. A separate measurement under each set of LINAC beam conditions was performed to identify the location, width, and shape of the gamma flash. The zero time was the center of a Gaussian fit to the gamma flash data.

### 4.5. Resolution function

Resolution broadening refers to the combined effects of the LINAC electron pulse width, the emission time in the moderator, the TOF channel width, and the effective thickness of the detector system. The resolution functions for thermal and epithermal capture, as well as epithermal transmission were entered as input to SAMMY using parameters obtained from previous fits using measurements of depleted uranium. (Barry, 2003; Leinweber et al., 2010; Barry et al., 2016). In the thermal transmission measurement the photomultiplier tube is in the neutron beam and must be represented by a more complex resolution function (Trbovich, 2003). A functional representation of the RPI resolution function was added to the SAMMY code in the late 1990's and continues to be used for thermal transmission data.

The flight path lengths for the various experiments are given in Table 1.

### 4.6. Sample impurities and temperature

Due to the high purity of the samples, no corrections for impurities were included in the SAMMY analysis (see Table 3).

The sample temperature assumed throughout the analysis was 293 K. This value was used in conjunction with the Debye temperature for rhenium (416 K at a temperature of 0 K) (Stewart, 1983) to obtain an effective temperature of 312.8 K. The effective temperature was used for Doppler broadening in the SAMMY analysis.

### 4.7. Radiation width determination

Radiation widths were fitted whenever a resonance included a significant quantity of scattering. The criterion of $\Gamma_\gamma / \Gamma_n < 5$ was adopted from Reference Barry (2003) to reflect sensitivity of a resonance to the value of the radiation width. Only for those resonances sensitive to the value of the radiation width, $\Gamma_\gamma$, is an uncertainty provided in the column labeled "$\Delta\ \Gamma_\gamma$" in Table 4 or Table 5; i.e., they satisfied the criterion.

For resonances with $\Gamma_\gamma / \Gamma_n \geq 5$, both transmission and capture

**Table 4**
Resonance parameters for $^{185}$Re compared with ENDF/B-VII.1 parameters. Two uncertainties are given for each parameter, the Bayesian uncertainty from the SAMMY fit and an external error, in brackets, which conveys the agreement among individual sample fits as described in Section 4.9.8.

| E, eV | ΔE | Eendf | $\Gamma_\gamma$ | Δ $\Gamma_\gamma$ | $\Gamma_\gamma$endf | $\Gamma_n$ | Δ $\Gamma_n$ | $\Gamma_n$endf | | J |
|---|---|---|---|---|---|---|---|---|---|---|
| | Bayesian[external] | | | Bayesian[external] | | | Bayesian[external] | isotope | | |
| −5.88 | 0.04[0.02] | −6.750 | 50 | | 55.500 | 37 | 0.7[1] | 46.286 | 185 | 3 |
| 2.1566 | 0.0001[0.0005] | 2.156 | 50 | | 54.900 | 2.95 | 0.002[0.03] | 2.829 | 185 | 3 |
| 5.91 | 0.0002[0.05] | 5.920 | 70 | | 69.000 | 0.24 | 0.0004[0.07] | 0.264 | 185 | 2 |
| 7.209 | 0.0002[0.002] | 7.220 | 50 | | 55.000 | 1.2 | 0.002[0.3] | 1.191 | 185 | 3 |
| 11.8542 | 0.0004[0.0005] | 11.880 | 50 | | 61.000 | 0.680 | 0.002[0.006] | 0.677 | 185 | 3 |
| 12.8297 | 0.0004[0.0005] | 12.900 | 70 | | 68.000 | 0.99 | 0.003[0.01] | 1.044 | 185 | 2 |
| 14.6114 | 0.0005[0.0008] | 14.640 | 70 | | 56.000 | 0.908 | 0.003[0.009] | 0.948 | 185 | 2 |
| 21.347 | 0.0007[0.002] | 21.300 | 70 | | 51.000 | 5.68 | 0.02[0.05] | 6.192 | 185 | 2 |
| 21.957 | 0.001[0.001] | 21.900 | 50 | | 55.569 | 0.393 | 0.003[0.002] | 0.394 | 185 | 3 |
| 26.546 | 0.001[0.001] | 26.600 | 50 | | 55.569 | 0.579 | 0.004[0.004] | 0.557 | 185 | 3 |
| 27.181 | 0.001[0.002] | 27.200 | 70 | | 55.569 | 0.747 | 0.005[0.008] | 0.672 | 185 | 2 |
| 29.528 | 0.001[0.002] | 29.480 | 50 | | 55.569 | 0.488 | 0.003[0.003] | 0.429 | 185 | 3 |
| 32.584 | 0.0006[0.001] | 32.530 | 67 | 1[5] | 51.000 | 27 | 0.1[1] | 27.429 | 185 | 3 |
| 36.593 | 0.001[0.0003] | 36.530 | 70 | | 55.569 | 1.044 | 0.009[0.008] | 0.948 | 185 | 2 |
| 41.440 | 0.0008[0.004] | 41.540 | 50 | | 55.569 | 11.2 | 0.05[0.9] | 8.486 | 185 | 3 |
| 45.384 | 0.002[0.0007] | 45.400 | 50 | | 55.569 | 0.421 | 0.004[0.002] | 0.454 | 185 | 3 |
| 47.743 | 0.004[0.004] | 47.680 | 70 | | 55.569 | 1.11 | 0.04[0.02] | 1.068 | 185 | 2 |
| 50.252 | 0.0008[0.002] | 50.220 | 66 | 0.8[2] | 51.000 | 18.1 | 0.08[0.3] | 18.840 | 185 | 2 |
| 51.504 | 0.0008[0.001] | 51.370 | 50 | | 51.000 | 26.6 | 0.09[0.6] | 24.000 | 185 | 3 |
| 54.972 | 0.001[0.002] | 55.100 | 50 | | 54.000 | 6.8 | 0.03[0.2] | 6.343 | 185 | 3 |
| 58.361 | 0.001[0.001] | 58.400 | 67 | 0.9[1] | 55.569 | 14.6 | 0.07[0.3] | 19.714 | 185 | 3 |
| 61.58 | 0.01[0.009] | 61.560 | 70 | | 55.569 | 0.36 | 0.02[0.004] | 0.348 | 185 | 2 |
| 62.851 | 0.001[0.001] | 62.860 | 50 | | 55.569 | 3.91 | 0.03[0.04] | 2.743 | 185 | 3 |
| 66.592 | 0.003[0.004] | 66.580 | 70 | | 55.569 | 1.12 | 0.02[0.02] | 0.948 | 185 | 2 |
| 70.521 | 0.001[0.002] | 70.490 | 70 | | 45.000 | 13.2 | 0.07[0.1] | 8.280 | 185 | 2 |
| 74.527 | 0.005[0.003] | 74.510 | 78 | 5[1] | 55.569 | 16.0 | 0.5[0.6] | 10.440 | 185 | 2 |
| 80.644 | 0.002[0.002] | 80.650 | 50 | | 55.569 | 6.17 | 0.06[0.05] | 4.371 | 185 | 3 |
| 81.069 | 0.003[0.003] | 81.010 | 50 | | 55.569 | 3.06 | 0.05[0.04] | 2.400 | 185 | 3 |
| 86.899 | 0.002[0.002] | 86.920 | 50 | | 55.569 | 8.95 | 0.09[0.06] | 6.171 | 185 | 3 |
| 87.29 | 0.02[0.01] | 87.310 | 70 | | 55.569 | 3.0 | 0.2[0.04] | 2.400 | 185 | 2 |
| 88.804 | 0.003[0.004] | 88.830 | 50 | | 55.569 | 2.11 | 0.03[0.06] | 1.457 | 185 | 3 |
| 93.187 | 0.003[0.001] | 93.180 | 50 | | 55.569 | 1.09 | 0.01[0.01] | 0.943 | 185 | 3 |
| 95.23 | 0.01[0.01] | 95.220 | 70 | | 55.569 | 2.6 | 0.2[0.03] | 3.600 | 185 | 2 |
| 98.305 | 0.002[0.003] | 98.300 | 50 | | 55.569 | 8.58 | 0.07[0.09] | 7.029 | 185 | 3 |
| 100.890 | 0.002[0.0008] | 100.800 | 70 | | 55.569 | 11.7 | 0.09[0.1] | 9.240 | 185 | 2 |

**Table 5**
Resonance parameters for $^{187}$Re compared with ENDF/B-VII.1 parameters. Two uncertainties are given for each parameter, the Bayesian uncertainty from the SAMMY fit and an external error, in brackets, which conveys the agreement among individual sample fits as described in Section 4.9.8.

| E, eV | ΔE | Eendf | $\Gamma_\gamma$ | Δ $\Gamma_\gamma$ | $\Gamma_\gamma$endf | $\Gamma_n$ | Δ $\Gamma_n$ | $\Gamma_n$endf | | J |
|---|---|---|---|---|---|---|---|---|---|---|
| | Bayesian[external] | | | Bayesian[external] | | | Bayesian[external] | isotope | | |
| −2.92 | 0.03[0.04] | −4.030 | 50 | | 56.800 | 8.7 | 0.2[0.3] | 17.571 | 187 | 3 |
| 4.407 | 0.0001[0.005] | 4.416 | 50 | | 54.600 | 0.31 | 0.0004[0.02] | 0.318 | 187 | 3 |
| 11.1143 | 0.0003[0.0004] | 11.140 | 70 | | 61.400 | 2.33 | 0.007[0.03] | 2.520 | 187 | 2 |
| 16.0258 | 0.0005[0.0009] | 16.000 | 70 | | 59.000 | 0.74 | 0.002[0.01] | 0.804 | 187 | 2 |
| 17.5190 | 0.0005[0.0003] | 17.480 | 50 | | 57.000 | 1.75 | 0.006[0.02] | 1.826 | 187 | 3 |
| 18.5340 | 0.0006[0.0005] | 18.510 | 70 | | 60.000 | 0.806 | 0.003[0.007] | 0.888 | 187 | 2 |
| 24.846 | 0.001[0.002] | 24.790 | 50 | | 60.343 | 0.0980 | 0.0008[0.0007] | 0.103 | 187 | 3 |
| 32.0083 | 0.0006[0.0007] | 31.970 | 50 | | 74.000 | 7.9 | 0.04[0.1] | 8.229 | 187 | 3 |
| 33.996 | 0.001[0.0006] | 33.980 | 70 | | 51.000 | 1.29 | 0.009[0.01] | 1.356 | 187 | 2 |
| 39.351 | 0.0007[0.001] | 39.350 | 50 | | 55.000 | 10.7 | 0.04[0.4] | 10.200 | 187 | 3 |
| 47.445 | 0.001[0.0009] | 47.390 | 70 | | 60.343 | 5.51 | 0.03[0.09] | 5.040 | 187 | 2 |
| 53.4406 | 0.0009[0.0006] | 53.360 | 50 | | 60.343 | 5.3 | 0.03[0.2] | 5.229 | 187 | 3 |
| 58.824 | 0.002[0.002] | 58.760 | 50 | | 60.343 | 2.06 | 0.02[0.01] | 2.143 | 187 | 3 |
| 60.9961 | 0.0009[0.0007] | 60.900 | 66 | 0.7[3] | 60.343 | 29.5 | 0.1[0.7] | 25.200 | 187 | 2 |
| 63.429 | 0.001[0.002] | 63.390 | 50 | | 60.343 | 1.95 | 0.01[0.01] | 1.920 | 187 | 3 |
| 69.408 | 0.001[0.001] | 69.390 | 68 | 0.8[2] | 60.000 | 29.1 | 0.1[0.7] | 31.200 | 187 | 2 |
| 73.644 | 0.001[0.001] | 73.550 | 53 | 0.5[5] | 49.000 | 63 | 0.3[2] | 57.429 | 187 | 3 |
| 74.842 | 0.002[0.007] | 74.810 | 74 | 3[4] | 63.000 | 28 | 0.5[2] | 17.520 | 187 | 2 |
| 77.909 | 0.002[0.0006] | 77.880 | 50 | | 60.343 | 1.28 | 0.01[0.003] | 1.286 | 187 | 3 |
| 78.843 | 0.002[0.001] | 78.790 | 50 | | 79.000 | 2.61 | 0.02[0.02] | 2.314 | 187 | 3 |
| 84.939 | 0.002[0.002] | 84.890 | 70 | | 65.000 | 11.0 | 0.06[0.1] | 8.400 | 187 | 2 |
| 87.480 | 0.003[0.002] | 87.390 | 50 | | 60.343 | 3.4 | 0.1[0.04] | 2.743 | 187 | 3 |
| 91.480 | 0.002[0.002] | 91.460 | 70 | | 60.343 | 2.27 | 0.02[0.01] | 2.400 | 187 | 2 |
| 95.598 | 0.002[0.002] | 95.520 | 66 | 0.8[4] | 60.343 | 65 | 0.3[2] | 51.429 | 187 | 3 |
| 98.892 | 0.003[0.004] | 98.790 | 50 | | 60.343 | 2.85 | 0.03[0.02] | 2.229 | 187 | 3 |

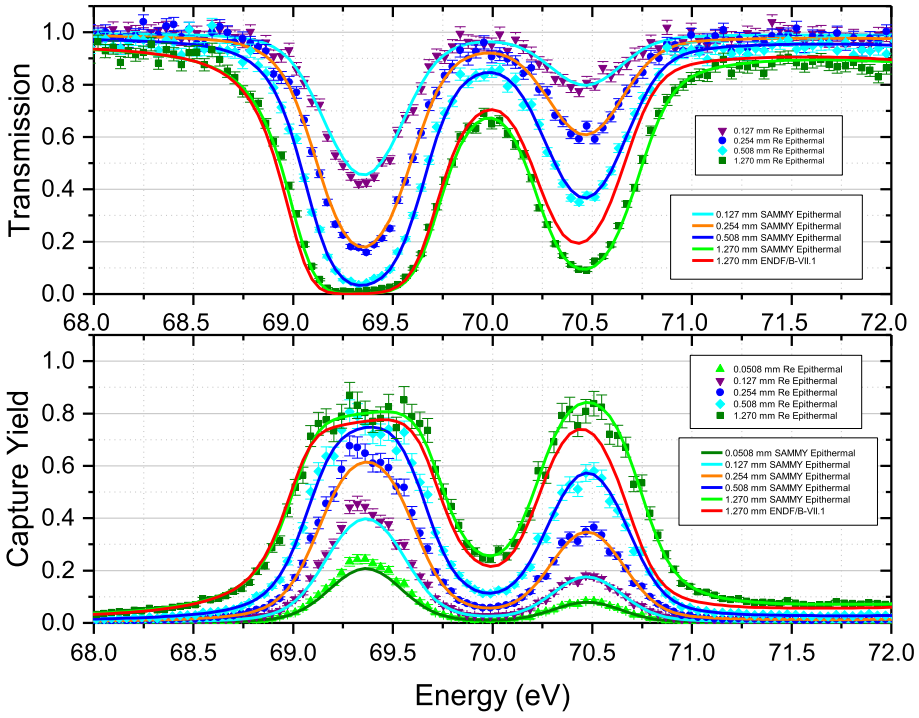


**Fig. 7.** NNL/RPI transmission and capture data in the epithermal region near 70 eV. A single set of resonance parameters were obtained from the SAMMY fit and used for the curves labeled "SAMMY fit". The line derived from ENDF/B-VII.1 for the 1.270 mm (50 mil) sample is included for comparison purposes. The NNL/RPI results indicate significant improvements over ENDF in the resonance near 70.5 eV.

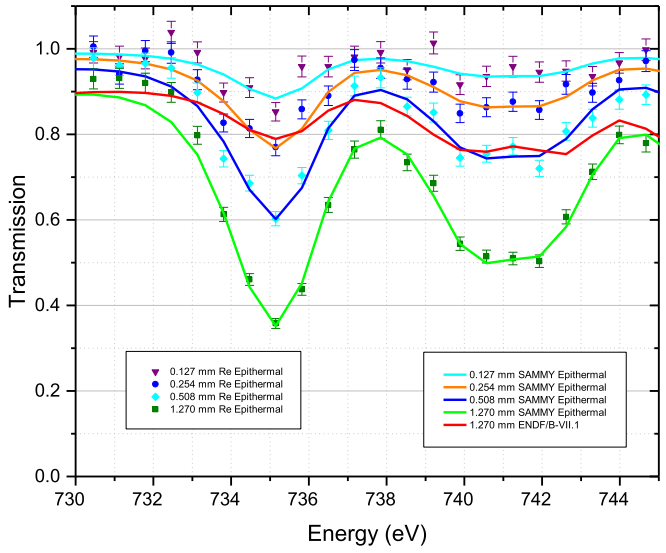


**Fig. 8.** NNL/RPI transmission and capture data in the epithermal region near 740 eV. A single set of resonance parameters were obtained from the SAMMY fit and used for the curves labeled "SAMMY fit". The line derived from ENDF/B-VII.1 for the 1.270 mm (50 mil) sample is included for comparison purposes. The NNL/RPI results indicate significant improvements over ENDF in the resonances near 740 eV.

measurements effectively measure the same quantity, $\Gamma_n$. For these mostly-capture resonances neither transmission nor capture data contain sufficient radiation width information. These resonances were assigned an average radiation width which was determined from all of the sensitive resonances with $\Gamma_\gamma / \Gamma_n < 5$. More detail on this method is given in References Barry (2003) and Leinweber et al. (2010). The average $\Gamma_\gamma$ for each isotope spin group (J = 2 or J = 3), $<\Gamma_\gamma>$, is shown in Table 6. These values, obtained from all of the $\Gamma_\gamma$-sensitive resonances, were assigned to all of the $\Gamma_\gamma$-insensitive resonances in Tables 4 and 5. The uncertainties in the average $\Gamma_\gamma$ values assigned to the $\Gamma_\gamma$-insensitive resonances were obtained from the standard deviation of the distribution of sensitive $\Gamma_\gamma$s; these uncertainty values are shown in Table 6. Each uncertainty value shown in Table 6 represents the uncertainty in the radiation width of an insensitive resonance for the applicable isotope spin group; notably, it is *not* the standard error of the mean, which would be the cited value divided by the square root of the number of sensitive resonances.

As a check, radiation widths were fitted from the data for the two lowest energy resonances despite the lack of sensitivity based on the $\Gamma_\gamma / \Gamma_n < 5$ criterion. Below 5 eV the observed resonance width is approximately equal to the Doppler-broadened width. The resolution function width is not significant at these low energies. The results of this check, $\Gamma_\gamma = 58$ meV for the 2.16 eV, J = 3, resonance in $^{185}$Re and $\Gamma_\gamma = 51$ meV for the 4.41 eV, J = 3, resonance in $^{187}$Re, were in agreement with the values shown in Tables 4 and 5.

### 4.8. Resonance integrals and thermal cross sections

Infinitely dilute capture resonance integrals (RIs) have been calculated from Equation (3),

$$RI = \int_{0.5eV}^{20MeV} \sigma_\gamma(E) \frac{dE}{E} \tag{3}$$

where $\sigma_\gamma(E)$ is the capture cross section in barns, Doppler broadened to 300K, and E is energy in eV. The cross sections were calculated from the resonance parameters shown in Tables 4 and 5. Above 1000 eV, ENDF/B-VII.1 cross sections were used. The resonance integrals were calculated using the NJOY (MacFarlane and Muir, 1994) and INTER (Dunford, 2001) programs. The results are shown in Table 7 in units of barns. Also, thermal capture cross

**Table 6**
Measured average $\Gamma_\gamma$, referred to as $< \Gamma_\gamma >$, and their uncertainties for rhenium. The average was obtained from the $\Gamma_\gamma$ -sensitive resonances and assigned to the insensitive resonances. The uncertainty is the standard deviation of the distribution of $\Gamma_\gamma$ values from resonances with $\Gamma_\gamma / \Gamma_n < 5$.

| Isotope Mass Number | S-Wave Total Angular Momentum, J | Average $\Gamma_\gamma$ $<\Gamma_\gamma>$ (meV) | Uncertainty in $<\Gamma_\gamma>$ (meV) |
|---|---|---|---|
| 185 | 2 | 70 | 20 |
| | 3 | 50 | 20 |
| 187 | 2 | 70 | 10 |
| | 3 | 50 | 10 |

**Table 7**
Capture resonance integrals of $^{185}$Re and $^{187}$Re. Resonance integrals for the rhenium isotopes are in units of barns. The NNL/RPI values were calculated from the measured resonance parameters shown in Tables 4 and 5 using the NJOY (Stewart, 1983) and INTER (MacFarlane and Muir, 1994) programs. The uncertainties were determined using a Monte Carlo method by sampling from the maximum uncertainties (either Bayesian or external) of the resonance parameters as shown in Tables 4 and 5 and repeating the NJOY and INTER runs using the sampled parameters until sufficient statistics were obtained. The percent changes of NNL/RPI relative to ENDF/B-VII.1[7] are also presented.

| | $^{185}$Re Capture Resonance Integral (barns) | $^{187}$Re Capture Resonance Integral (barns) |
|---|---|---|
| NNL/RPI | 1800 ± 20 | 310 ± 3 |
| ENDF/B-VII.1(Chadwick et al., 2011) | 1738 | 301 |
| Percent change from ENDF/B-VII.1 | +(4 ± 1)% | +(3 ± 1)% |

sections and thermal total cross sections were calculated from resonance parameters using the NJOY and INTER programs, and the results are presented in Table 8 including comparisons of the current measurements to ENDF/B-VII.1 and to the results of Arboccò et al. (2013). The capture resonance integral of $^{185}$Re has increased by (4 ± 1)% compared to ENDF/B-VII.1. The thermal capture cross section and the thermal total cross section of $^{185}$Re have each decreased by (2 ± 2)%. compared to ENDF/B-VII.1. The capture resonance integral of $^{187}$Re has increased (3 ± 1)% relative to ENDF/B-VII.1, while the thermal capture cross section has decreased by (3 ± 4)% and the thermal total cross section has decreased by (6 ± 5)%. Considering the uncertainties, none of the indicated changes in thermal cross sections for either rhenium isotope represents a statistically significant change from ENDF/B-VII.1.

The uncertainties in the resonance integrals given in Table 7 and the thermal capture and thermal total cross sections given in Table 8 were determined using a Monte Carlo method by sampling from normal distributions spanning the largest of the uncertainties of the resonance parameters as shown in Tables 4 and 5 and repeating the NJOY and INTER runs using the sampled parameters until sufficient statistics were obtained.

### 4.9. Components of resonance parameter uncertainties

The components of resonance parameter uncertainty were counting statistics, background, normalization, time zero, pulse width, resolution function, sample thickness, isotopic abundance, effective temperature, and flight path length. The components of uncertainty correspond to the important aspects of the analysis described in Sections 4.2 through 4.6. Some of the uncertainties (e.g., counting statistics) were explicitly propagated with the measured transmission and capture yield data results; the rest were separately propagated using the PUP (Propagated Uncertainty Parameter) feature of SAMMY. The Bayesian SAMMY uncertainties are given in the second, sixth, and tenth columns of Tables 4 and 5. External uncertainties (see Section 4.9.8) are given in brackets, [], as the third, seventh, and eleventh columns of Tables 4 and 5 and are described in Section 4.9.8.

#### 4.9.1. Uncertainty in background

For transmission data the uncertainty in the background was propagated from the counting statistics in the notch runs and the quality of the background function fit into each data point. Additionally, an uncertainty was propagated based on the agreement of the background function normalized at the fixed notch resonance to the background indicated in the black rhenium resonance at 2.16 eV. The background uncertainty propagated in the SAMMY analysis was 5.4% for epithermal transmission and 6.9% for thermal transmission.

For capture measurements two empty sample holders were placed in the sample sequence throughout the experiments to measure background. The difference between the signals from these two empty sample holders was used as an estimate of the uncertainty of the background in the neutron capture measurements; this uncertainty was determined to be 6% of the measured background for epithermal capture and 4% of the measured background for thermal capture. These values were validated by observing the measured capture yield values between resonance peaks, where non-zero values can serve to quantify the error in the background.

**Table 8**
Thermal cross sections for the rhenium isotopes in units of barns. The NNL/RPI values were calculated from the measured resonance parameters shown in Tables 4 and 5 using the NJOY (Stewart, 1983) and INTER (MacFarlane and Muir, 1994) programs. The uncertainties were determined using a Monte Carlo method by sampling from the maximum uncertainties (either Bayesian or external, whichever is larger) of the resonance parameters as shown in Tables 4 and 5 and repeating the NJOY and INTER runs using the sampled parameters until sufficient statistics were obtained. The percent changes of NNL/RPI relative to ENDF/B-VII.1 (Chadwick et al., 2011) are also presented.

| | $^{185}$Re | | $^{187}$Re | |
|---|---|---|---|---|
| | Thermal Capture Cross Section (barns) | Thermal Total Cross Section (barns) | Thermal Capture Cross Section (barns) | Thermal Total Cross Section (barns) |
| NNL/RPI | 110 ± 2 | 118 ± 2 | 75 ± 3 | 82 ± 4 |
| Arboccò et al. 2013 | 111.6 ± 1.1 | N/A | 74.6 ± 1.4 | N/A |
| ENDF/B-VII.1 (Chadwick et al., 2011) | 112 | 121 | 77 | 87 |
| NNL/RPI Percent change from ENDF/B-VII.1 | - (2 ± 2)% | - (2 ± 2)% | - (3 ± 4)% | - (6 ± 5)% |

#### 4.9.2. Uncertainty in normalization

The normalization for transmission data was set to unity (1.0) and not fitted in the SAMMY analysis. An uncertainty for the normalization value of unity applied to the transmission data was derived from the statistical combination of the potential scattering radius uncertainty (discussed in Section 4.11) and fluctuations indicated by beam monitor instability. Each sample was cycled in and out of the beam during the measurement runs to reduce the effect of beam monitor fluctuations, but monitor normalization uncertainties as high as 2.6% were observed. The final normalization uncertainties were calculated on an individual sample basis for each measurement type. The results of all samples were in close agreement. For epithermal transmission, a final normalization uncertainty value of 3.9% was propagated in the SAMMY analysis for all samples. A final normalization uncertainty value of 3.8% was propagated in the SAMMY analysis for all thermal transmission samples.

For the capture measurements the neutron flux was initially normalized to the black rhenium resonance at 2.16 eV. SAMMY was subsequently used to fit capture yield normalization using fits derived from transmission data to obtain an additional normalization correction factor. Normalization uncertainties were derived for each sample and measurement type using beam monitor stability. The normalization uncertainties propagated in the SAMMY analysis for epithermal capture data ranged from 1.7% to 1.8%, and for thermal capture data ranged from 0.9% to 2.6%.

#### 4.9.3. Uncertainty in the zero time measurement

As previously discussed, the zero time was obtained from the center value of a Gaussian fit of data obtained during measurements of the gamma flash. The uncertainty of the zero time was the uncertainty in the center of the Gaussian fit to the gamma flash data. The resultant zero time uncertainty values were 0.4 ns for epithermal transmission, 0.1 ns for epithermal capture, 18 ns for thermal transmission, and 51 ns for thermal capture. The thermal measurements have higher uncertainties because the gamma flash pulse shape is asymmetric and there are fewer counts. However, the effect of the higher zero time uncertainties on energy in the thermal region is very small.

#### 4.9.4. Uncertainty in the burst width

Measurements of the gamma burst produced at the beginning of each LINAC pulse were measured and analyzed to determine the width and uncertainty in the width of the pulse in units of time. Pulse widths are given in Table 1. The electron pulse appears Gaussian for the narrow pulses used in the epithermal measurements. The uncertainties in the full width half maximum (FWHM) of the gamma flash pulse widths were less than 2 ns The wide pulses used in the thermal measurements are irregularly shaped and have a larger uncertainty, up to 15% of pulse width. Experience has shown that these uncertainties do not contribute significantly to resonance parameter uncertainties in low energy resonances.

#### 4.9.5. Uncertainty in the resolution function

The uncertainties in resolution function parameters have been obtained from measurements of uranium in the various measurement configurations (Barry, 2003; Leinweber et al., 2010; Trbovich, 2003; Barry et al., 2016) and were propagated into all of the resonance parameter uncertainties given in Tables 4 and 5.

#### 4.9.6. Uncertainty in the sample thickness

Sample thickness uncertainty values were calculated for each individual sample. As discussed in Section 2.1, the sample thickness uncertainties were dominated by the uncertainties in sample diameter measurements, as opposed to the smaller uncertainties in the mass measurements, which used an electronic balance. Sample thickness uncertainty values ranged from 9E-8 atoms/barn (0.0254 mm (1 mil) sample) to 1E-5 atoms/barn (2.540 mm (100 mil) sample). These values were included in the SAMMY analysis.

The uniformity of thickness of the 0.0254 mm and the 0.0508 mm thick samples was measured with a micrometer at multiple locations. The resulting thickness distributions were included in the analysis using the non-uniform feature of SAMMY.

#### 4.9.7. Uncertainty in the flight path length

Flight path lengths are given in Table 1. An uncertainty value of 0.0055 m was applied to all flight path lengths. This uncertainty value is based on the mean free path of a neutron in the moderator thickness of the targets. This value was included in the SAMMY analysis.

#### 4.9.8. External uncertainties from individual sample fits

An external uncertainty is associated with the variability between independent measurements of the same quantity. The external uncertainty is a weighted, by SAMMY uncertainties, standard deviation of the distribution of values from the individual sample fits. SAMMY does not account for the external uncertainties between measurements. The uncertainty given in brackets, [ ], for each resonance in Tables 4 and 5 is the external uncertainty between individual sample fits. An ensemble of individual sample fits does not take advantage of the Bayesian treatment of a SAMMY multi-sample fit.

The external uncertainties apply to the weighted, by SAMMY uncertainties, average of each resonance parameter from individual sample fits. These averages agree with the SAMMY multi-sample Bayesian central values within the SAMMY uncertainties.

### 4.10. Nuclear statistics

#### 4.10.1. Average level spacing

A staircase plot of level density is shown in Fig. 9 for $^{185}$Re and in Fig. 10 for $^{187}$Re. The average level spacing, $D_0$, is the inverse of the slope of each straight line fit up to the point where $D_0$ falls below a constant value indicating that levels are being missed in the resonance analysis. Since no new resonances have been identified in

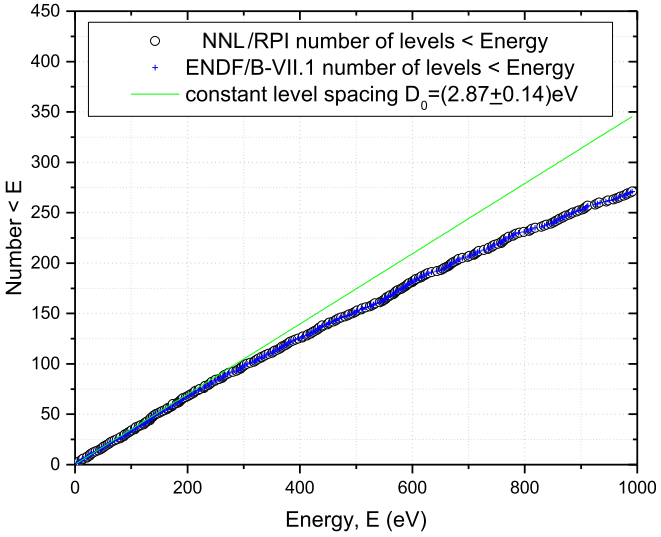


**Fig. 9.** Staircase plot of level density for $^{185}$Re. The line of constant level density corresponds to an average level spacing, $D_0 = 2.87 \pm 0.14$ eV, as documented in the Atlas (Mughabghab, 2006).

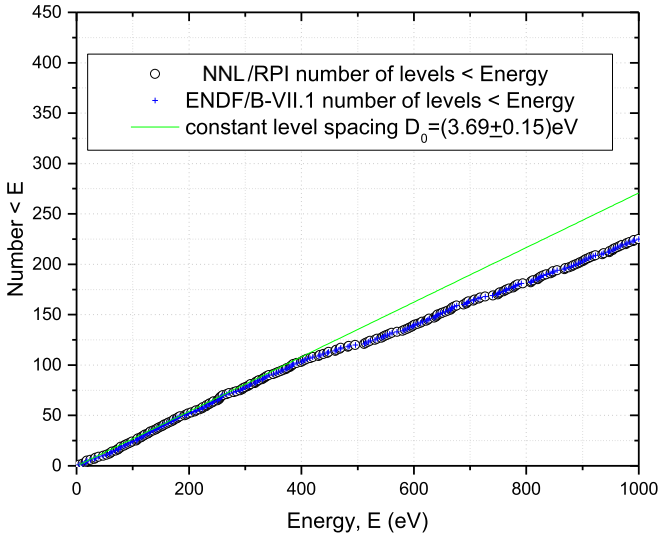


**Fig. 10.** Staircase plot of level density for $^{187}$Re. The line of constant level density corresponds to an average level spacing, $D_0 = 3.69 \pm 0.15$ eV, as documented in the Atlas (Mughabghab, 2006).

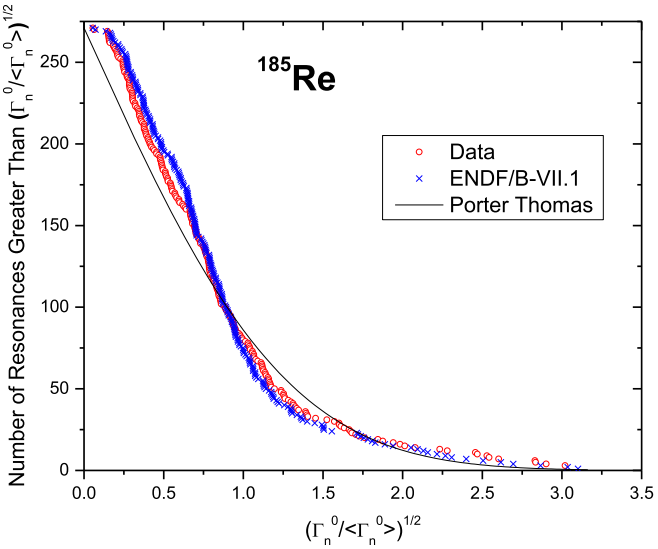


**Fig. 11.** Cumulative reduced neutron width distributions for the present measurements and ENDF/B-VII.1 of $^{185}$Re compared to Porter Thomas distributions. The new data generally show improvement compared to theory except for the strongest resonances.

either rhenium isotope as a result of this work, the lines of constant level density were not explicitly evaluated as part of this analysis. Instead, the lines of constant level density shown in Fig. 9 and Fig. 10 correspond to the average level spacing documented in the Atlas (Mughabghab, 2006) with corresponding values of $D_0 = 2.87 \pm 0.14$ eV for $^{185}$Re and $D_0 = 3.69 \pm 0.15$ eV for $^{187}$Re (see Table 9).

### 4.10.2. Neutron width distributions

Cumulative reduced neutron width distributions for the present measurements and ENDF/B-VII.1 are shown in Fig. 11 and Fig. 12. The figures compare the distributions to those predicted from Porter-Thomas theory (Porter & Thomas, 1956). Each data point shown in Fig. 11 and Fig. 12 was calculated using the average value, $\langle\Gamma_n^0\rangle$, specific to each spin group. Then the population of ratios, $\Gamma_n^0/\langle\Gamma_n^0\rangle$, were plotted for each isotope. The new data show some improvements compared to theory, particularly for the weaker resonances.

Neutron strength functions, $S_0$, were measured for both $^{185}$Re and $^{187}$Re. The value of the strength function is dependent upon the energy region analyzed. For this analysis, strength functions were calculated over the energy regions where the resonance level density corresponded with the line of constant level density (see Fig. 9 and Fig. 10). For $^{185}$Re, this was judged to include the energy region up to 200 eV. For $^{187}$Re, this was judged to include the energy region up to 270 eV. The measured values are compared to those of ENDF/B-VII.1 (calculated over the same energy regions) in Table 10. As shown in the table, neither the measured results nor the ENDF/B-VII.1 results show good agreement with the values documented in the Atlas (Mughabghab, 2006); although the Atlas does not indicate the specific energy region to calculate strength functions for the rhenium isotopes. The s-wave strength for $^{185}$Re is smaller than the Atlas value, while the s-wave strength for $^{187}$Re is larger than the corresponding Atlas value.

**Table 9**
Statistics of the level density and neutron width distributions of the rhenium isotopes.

| Level Densities | | |
|---|---|---|
| | $D_0$, eV, NNL/RPI | $D_0$, eV, Atlas (Mughabghab, 2006) |
| $^{185}$Re | ** | 2.87 ± 0.14 |
| $^{187}$Re | ** | 3.69 ± 0.15 |
| Reduced neutron width distributions, $^{185}$Re, DF = degrees of freedom of a $\chi^2$ distribution based on the variance of the reduced neutron widths. Each reduced width was divided by the average from its own spin state ($\langle\Gamma_n^0\rangle$), then the ratios grouped by isotope. | | |
| | $\langle\Gamma_n^0\rangle$ (meV) | DF = $2/\mathrm{var}(\Gamma_n^0/\langle\Gamma_n^0\rangle)$ |
| $^{185}$Re NNL/RPI | 1.87 (J = 2) | 0.92 |
| | 1.39 (J = 3) | |
| $^{185}$Re ENDF/B-VII.1 | 1.49 (J = 2) | 0.96 |
| | 1.14 (J = 3) | |
| Reduced neutron width distributions, $^{187}$Re, see note for $^{185}$Re above. | | |
| | $\langle\Gamma_n^0\rangle$ (meV) | DF = $2/\mathrm{var}(\Gamma_n^0/\langle\Gamma_n^0\rangle)$ |
| $^{187}$Re NNL/RPI | 0.10 (J = 2) | 1.92 |
| | 0.07 (J = 3) | |
| $^{187}$Re ENDF/B-VII.1 | 2.10 (J = 2) | 1.39 |
| | 1.56 (J = 3) | |

**The current analysis did not identify any new resonances. As a result, level densities were not explicitly evaluated.

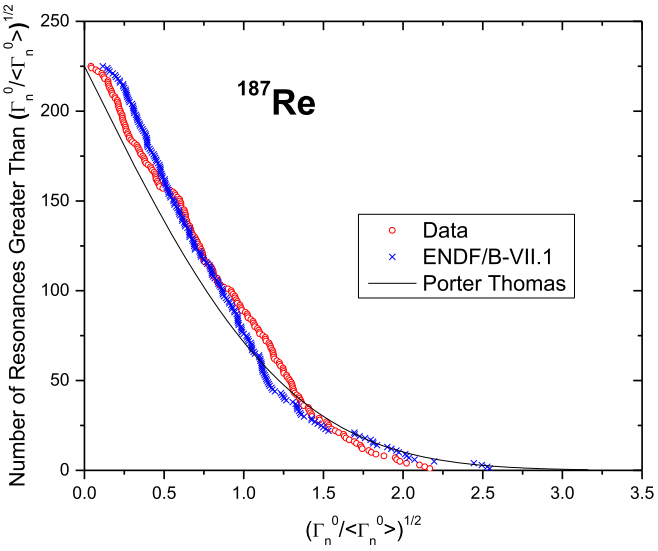


**Fig. 12.** Cumulative reduced neutron width distributions for the present measurements and ENDF/B-VII.1 of $^{187}$Re compared to Porter Thomas distributions. The new data generally show improvement compared to theory except for the strongest resonances.

**Table 10**
Neutron strength function, $S_0$, for the naturally-occurring isotopes of Re. NNL/RPI values and ENDF/B-VII.1 values were analyzed over the energy region up to 200 eV for $^{185}$Re and 270 eV for $^{187}$Re. The energy region used to calculate the strength functions in the Atlas of Neutron Resonances was not specified. The uncertainties for ENDF are not included (Mughabghab, 2006) since no uncertainties are available for the neutron widths.

| | $S_0$ $^{185}$Re ($10^{-4}$ x meV$^{-1/2}$) | $S_0$ $^{187}$Re ($10^{-4}$ x meV$^{-1/2}$) |
|---|---|---|
| NNL/RPI | 1.5 ± 0.1 | 3.1 ± 0.1 |
| ENDF/B-VII.1 | 1.5 | 2.6 |
| Atlas of Neutron Resonances | 2.16 ± 0.14 | 2.43 ± 0.28 |

#### 4.10.3. Radiation width distributions

The neutron transmission and capture measurements revealed radiation width information from too few resonances to present radiation width distributions. Radiation widths were varied according to the criteria discussed in Section 4.7 and the results are shown in Tables 4 and 5.

### 4.11. Nuclear radii

The nuclear radii used in the final fits of rhenium data were analyzed using the data between resonances in transmission over eight regions below 70 eV. The weighted average and uncertainty for the nuclear radius was found to be 9.3 ± 0.2 fm, which was applied to both rhenium isotopes. This value represents a 7% increase from the Atlas (Mughabghab, 2006) value of 8.7 fm and an 18% increase from the ENDF/B-VII.1 value of 7.9 fm.

The channel radii that were used for penetrabilities and phase shifts (7.79 fm for $^{185}$Re, and 7.81 fm for $^{187}$Re) were calculated using equation (3) (Herman & Trkov, 2010).

$$a = 1.23 \text{ x } AWRI^{1/3} + 0.8 \quad (3)$$

Where:

$a$ is in fm, and

*AWRI* is the ratio of the atomic weight to the mass of the neutron.

## 5. Discussion and conclusions

Transmission and capture measurements were performed and analyzed. Experiments tailored separately to the thermal and epithermal energy regions were performed. Natural rhenium samples were measured. Resonance parameters were extracted using the Bayesian analysis code SAMMY. The significant features of this measurement and analysis were in the use of multiple sample thicknesses, the treatment of radiation widths and uncertainties, and improved energy resolution. This measurement establishes a refinement of the resonance parameters given in ENDF/B-VII.1.

Fig. 4 through Fig. 8 show the quality of the fits to the data. Fig. 4 is an overview of the data below 4 eV. Fig. 5 shows the energy region from 3 to 30 eV. Fig. 6 shows the region from 30 to 1000 eV. Fig. 7 shows a close-up of a portion of the energy region near 70 eV, where the data show significant improvements over ENDF in the resonance near 70.5 eV. Fig. 8 shows a close-up of a portion of the energy region near 740 eV, where the data show significant improvements over ENDF in the resonances near 740 eV. The staircase plots in Fig. 9 and Fig. 10 show that many more levels are needed in the region shown in Fig. 6 for $^{185}$Re and $^{187}$Re. The fits in Fig. 6 could be improved with the addition of those levels.

The current estimates of radiation width uncertainties were based upon the conservative method described in Section 4.7. This method addressed the issue of insensitivity of transmission data to radiation widths. Rather than relying on fitted results to data which contained very little radiation width information, a method was employed to determine accurate radiation widths of a few sensitive resonances where measured radiation width information was found in the data. These data-determined average radiation widths were assigned to the insensitive resonances. A distribution of radiation widths was determined for each isotope. The standard deviation of each distribution was used as the uncertainty on the average radiation width, see Table 6.

The determination of transmission background is a crucial task in any resonance parameter analysis. Separate background measurements were made using a suite of notch filters, and a fixed notch was used to provide a definitive background point in the data.

Detailed uncertainty information was compiled for background, normalization, time zero, pulse width, resolution function, sample thickness, isotopic abundance, effective temperature, and flight path length; see Section 4.9. The Propagated Uncertainty Parameter feature of the SAMMY code was used to propagate all known sources of uncertainty into the final results.

Conclusions of the current measurement include an increase of (4 ± 1)% in the capture resonance integral for $^{185}$Re and an increase of (3 ± 1)% in the capture resonance integral for $^{187}$Re from ENDF/B-VII.1. Small decreases were observed in the thermal capture cross section and thermal total cross section of both isotopes, but the changes from ENDF/B-VII.1 are not statistically significant.

## Acknowledgements

The authors gratefully acknowledge the contributions and support provided by the RPI LINAC operations staff (P. Brand, M. Gray, M. Strock, and A. Kerdoun), as well as NNL and RPI researchers (J. Burke, N. Drindak, and F. Saglime) during the rhenium measurements.

## References


Barry, D.P., 2003. Neodymium Neutron Transmission and Capture Measurements and Development of a New Transmission Detector. PhD Thesis. Rensselaer Polytechnic Institute.

Barry, D.P., Rapp, M.J., Block, R.C., Epping, B.E., Leinweber, G., Danon, Y., Daskalakis, A., Blain, E., McDermott, B., 2016. $^{236}$U resonance parameters at 5.467 eV from neutron transmission measurements using thin liquid samples. Prog. Nucl. Energy 86, 11.

Baum, E.M., Ernesti, M.C., Knox, H.D., Miller, T.R., Watson, A.M., Travis, S.D., 2010. Chart of the Nuclides, seventeenth ed. Bechtel Marine Propulsion Corporation.

Block, R.C., Marano, P.J., Drindak, N.J., Feiner, F., Seemann, K.W., Slovacek, R.E., 1988. A multiplicity detector for accurate low-energy neutron capture measurements. In: Proc. Int. Conf. Nuclear Data for Science and Technology, May 30-June 3. Mito, Japan, 383.

Busby, J.T., Leonard, K.J., Zinkle, S.J., 2007. Radiation damage in molybdenum-rhenium Alloys for space reactor applications. J. Nucl. Mater. 366, 388–406.

Chadwick, M.B., et al., 2011. ENDF/B-VII.1: nuclear data for science and technology: cross sections, covariances, fission product yields and decay data. Nucl. Data Sheets 112, 2887.

Craft, A.E., O'brien, R.C., Howe, S.D., King, J.C., 2014. Submersion criticality safety of tungsten-rhenium urania cermet fuel for space propulsion and power applications. Nucl. Eng. Des. 273, 143–149.

Danon, Y., Block, R.C., 2002. Minimizing the statistical error of resonance parameters and cross sections derived from transmission measurements. Nucl. Instrum. Methods Phys. Res. A 485, 585–595.

Danon, Y., Block, R.C., 2005. Minimizing the statistical error in capture cross section measurements. Nucl. Instrum. Methods Phys. Res. A 544 (3), 659.

Danon, Y., Slovacek, R.E., Block, R.C., 1993. The enhanced thermal neutron target at the RPI LINAC. Proc. Am. Nucl. Soc. Annu. Meet. (San Diego, CA) 68, 473.

Danon, Y., Slovacek, R.E., Block, R.C., 1995. Design and construction of a thermal neutron target for the RPI LINAC. Nucl. Instrum. Methods Phys. Res. A 352, 596.

Dunford, C.L., 2001. ENDF Utility Codes Release 6.12. Informal Report.

Epping, B.E., Leinweber, G., Barry, D.P., Rapp, M.J., Block, R.C., Donovan, T.J., Danon, Y., Landsberger, S., 2017. Tabulated Rhenium Resonance Parameters from Neutron Capture and Transmission Measurements in the Energy Range 0.01 eV to 1 keV. U.S. Department of Energy Office of Scientific and Technical Information.

Arboccò, F. Farina, Vermaercke, P., Smits, K., Sneyers, L., Strijckmans, K., 2013. Experimental determination of $k_0$, $Q_0$, $\bar{E}_r$ factors and neutron cross-sections for 41 isotopes of interest in Neutron Activation Analysis. J. Radioanalytical Nucl. Chem. 296 (2), 931.

Friesenhahn, S.J., Gibbs, D.A., Haddad, E., Fröhner, F.H., Lope, W.M., 1967. Neutron capture cross sections and resonance parameters of rhenium from 0.01 eV to 30 keV. J. Nucl. Energy 22 (#4), 191.

Guan, W., Nogami, S., Fukuda, M., Hasegawa, A., 2016. Tensile and fatigue properties of potassium doped and rhenium containing tungsten rods for fusion reactor applications. Fusion Eng. Des. 109-111, 1538–1542.

Herman, M., Trkov, A., July 2010. ENDF-6 Formats Manual. CSEWG Document ENDF-102, Report BNL-90365–2009, Rev. 1.

Ideno, K., Asami, T., Nakajima, Y., Ohkubo, M., Fuketa, T., 1972. Slow neutron resonances of rhenium. J. Nucl. Sci. Technol. 9 (#5), 261.

Igo, G., 1955. Slow neutron resonances in rhenium. Phys. Rev. 100, 1338.

Larson, N.M., October 2008. Updated Users' Guide for SAMMY: Multilevel R-matrix Fits to Neutron Data Using Bayes' Equations. ORNL/TM-9179/R8 ENDF-364/R2. Oak Ridge National Laboratory.

Leinweber, G., Burke, J.A., Knox, H.D., Drindak, N.J., Mesh, D.W., Haines, W.T., Ballad, R.V., Block, R.C., Slovacek, R.E., Werner, C.J., Trbovich, M.J., Barry, D.P., Sato, T., 2002. Neutron capture and transmission measurements and resonance parameter analysis of samarium. Nucl. Sci. Eng. 142, 1.

Leinweber, G., Barry, D.P., Burke, J.A., Drindak, N.J., Danon, Y., Block, R.C., Francis, N.C., Moretti, B.E., 2010. Resonance parameters and uncertainties derived from epithermal neutron capture and transmission measurements of natural molybdenum. Nucl. Sci. Eng. 164, 287.

MacFarlane, R.E., Muir, D.W., 1994. The NJOY Nuclear Data Processing System Version 91. LA-12740-M. Los Alamos National Laboratory.

Melkonian, E., Havens, W.W., JR, Rainwater, L.J., 1953. Slow neutron velocity spectrometer studies. V, Re, Ta, Ru, Cr, Ga. Phys. Rev. 92, 702.

Mughabghab, S.F., 2006. Atlas of Neutron Resonances, fifth ed. Elsevier, New York.

Namenson, A.I., Stolovy, A., Harvey, J.A., 1976. Neutron resonances in 185Re and 187Re. Nucl. Phys. A266 (#1), 83.

Overberg, M.E., Moretti, B.E., Slovacek, R.E., Block, R.C., 1999. Photoneutron target development for the RPI linear accelerator. Nucl. Instrum. Methods Phys. Res. A 438, 253.

Porter, C.E., Thomas, R.G., 1956. Fluctuations of nuclear reaction widths. Phys. Rev. 104, 483.

Stewart, G.R., 1983. Measurement of low-temperature specific heat. Rev. Sci. Instrum. 54 (1), 1.

Syme, D.B., 1982. The black and white-filter method for background determination in neutron time-of-flight spectrometry. Nucl. Instrum. Methods 198, 357.

Trbovich, M.J., 2003. Hafnium Neutron Cross Sections and Resonance Analysis. PhD Thesis. Rensselaer Polytechnic Institute.

Vertebnyi, V.P., Vlasov, M.F., Kirilyuk, A.L., Kolotyi, V.V., Pisanko, Z.H.I., Trofimova, N.A., 1965. Total cross sections of Re185 and Re187. Sov. At. Energy 19 (#3), 1162 (translated from Atomnaya Énergiya).

Weast, R.C., Astle, M.J., Beyer, W.H., 1987. CRC Handbook of Chemistry and Physics, 67th Edition. CRC Press, Inc.